Developing hierarchically porous MnOx/NC hybrid nanorods for oxygen reduction and evolution catalysis

Pandey, J.; Hua, B.; Ng, W.; Yang, Y.; van der Veen, K.; Chen, J.; Geels, N.J.; Luo, J.-L.; Rothenberg, G.; Yan, N.

DOI
10.1039/C7GC00147A

Publication date
2017

Document Version
Final published version

Published in
Green Chemistry

An article presented by Dr. Ning Yan *et al.* from the Sustainable Chemistry RPA of the University of Amsterdam, The Netherlands.

Developing hierarchically porous MnOx/NC hybrid nanorods for oxygen reduction and evolution catalysis

Starting from abundant precursors and using a simple synthesis approach, we report a good bifunctional oxygen electro-catalyst. The composite nanorods, comprising manganese oxides and nitrogen-doped carbon, have hierarchical porosity. The nitrogen-doped carbon forms a contiguous 3D network, connecting all the isolated MnO_x nanoparticles and ensuring superior electrical conductivity. This hybrid is among the best non-noble-metal ORR/OER catalysts in alkaline media, outperforming even Pt and RuO_2 catalysts.

As featured in:

See Ning Yan *et al.*, *Green Chem.*, 2017, **19**, 2793.

ROYAL SOCIETY OF CHEMISTRY

rsc.li/greenchem

Registered charity number: 207890

Green Chemistry

PAPER

View Article Online
View Journal | View Issue

Cite this: *Green Chem.*, 2017, **19**, 2793

Developing hierarchically porous MnO_x/NC hybrid nanorods for oxygen reduction and evolution catalysis†

Jay Pandey,[a] Bin Hua,[b] Wesley Ng,[a] Ying Yang,[c] Koen van der Veen,[a] Jian Chen,[d] Norbert J. Geels,[a] Jing-Li Luo,[b] Gadi Rothenberg[a] and Ning Yan*[a]

Received 13th January 2017,
Accepted 15th March 2017

DOI: 10.1039/c7gc00147a

rsc.li/greenchem

Electrochemical oxygen reduction and evolution reactions (ORR and OER) play a vital role in the field of energy conversion and storage. The problem is that both processes are sluggish, requiring precious-metal catalysts. Here, starting from abundant precursors and using a simple synthesis approach, we report the preparation of a good bifunctional oxygen electro-catalyst: a composite nanorod of manganese oxides and nitrogen-doped carbon. This material has hierarchical porosity, facilitating the mass transfer within the electrode. The nitrogen-doped carbon forms contiguous 3D network, connecting the isolated MnO_x nanoparticles and ensuring superior electrical conductivity. Importantly, the MnO_x particles contain manganese of mixed oxidation states; aligned with the nitrogen-doped carbon, this hybrid is among the best non-noble-metal ORR/OER catalysts in alkaline media, outperforming even Pt and RuO_2 catalysts.

Introduction

The ever-increasing quest for sustainability calls for green energy solutions.[1–5] In this context, the oxygen reduction reaction (ORR) and the oxygen evolution reaction (OER) have become a focus of attention. They play pivotal roles in various emerging energy conversion and storage devices including reversible fuel cells and metal-air batteries.[6–9] However, efficient ORR/OER is often catalyzed by noble-metal catalysts,[9–12] posing a challenge for real-life applications. Besides, good ORR catalysts often lack OER activity and *vice versa*.[13–15] This is problematic when switching the charging/discharging mode of the batteries or transforming fuel cells into electrolysis cells. Thus, inexpensive bifunctional ORR/OER catalysts feature high on industrial wish lists.

There are a number of promising alternatives indeed. For instance, transition metal oxides, including simple and perovskite oxides,[5,16–18] demonstrate superior intrinsic bifunctional activity; several recent review papers have well summarized the research progress made to date.[5,16,18] Among all the candidates, manganese oxide catalysts have attracted much attention.[13,18–22] Manganese is an earth-abundant metal, which forms a variety of oxide compounds, some of which have demonstrated great activities in ORR and/or OER.[18,23] But their poor electrical conductivity may limit the electrochemical performance.[13,21,24,25] Another typical example is the nitrogen-doped carbons that are good ORR catalysts with excellent conductivity as shown by many researchers,[26–29] but their susceptibility to passivation at high anodic potential may challenge their use in OER.[30,31]

In addition, optimizing the microstructure and morphology of the electrocatalysts is another promising approach for boosting their activities. It generates more active sites, forms composites, tunes the electronic structure, and creates hierarchical porosity (*e.g.*, connected meso-/macro-pores).[7,10,13–15,27,28,32–34] Nonetheless, making such structures is not an easy task. The synthetic routes are usually complicated and costly. In many cases, expensive and/or toxic reagents are also required.[13–15,28,35–37] For these reasons, concerns arise regarding the scalable synthesis.

In this work, we report a green synthesis of a bifunctional oxygen catalyst comprising MnO_x and N-doped carbon. Starting from two simple precursors (nitrilotriacetic acid and manganese acetate), this synthesis produces hybrid nanorods using a facile approach. The unique nano-structure grants excellent activity towards both ORR and OER in alkaline media, opening opportunities for practical application.

[a]*Van't Hoff Institute for Molecular Sciences, University of Amsterdam, Science Park 904, 1098 XH Amsterdam, The Netherlands. E-mail: n.yan@uva.nl; Tel: +31 20 525 6468*
[b]*Department of Chemical and Materials Engineering, University of Alberta, T6G 1K9, Edmonton, AB, Canada*
[c]*Department of Mechanics and Engineering Structure, Wuhan University of Technology, 430070 Wuhan, China*
[d]*National Institute for Nanotechnology, National Research Council of Canada, T6G 2M9, Edmonton, AB, Canada*

† Electronic supplementary information (ESI) available: Experimental details and additional materials characterization and electrochemical test data. See DOI: 10.1039/c7gc00147a

Results and discussion

Fig. 1 illustrates the synthesis procedure of the MnO_x/N-doped carbon hybrid nanorod. After the hydrothermal treatment of two precursors, nitrilotriacetic acid (NTA) and manganese acetate, at 180 °C, a rod-like salt (MnNTA) was crystallized and precipitated. Pyrolysis of washed MnNTA nanorods at 900 °C in Ar yielded MnO/N-doped carbon hybrid rods (MnO/NC). A final mild-oxidation at 200 °C in air converted the surface of MnO to MnO_x (hereafter MnO_x/NC), yet without oxidizing the NC matrix. Fig. S1† compares the results of the thermogravimetric analysis and differential scanning calorimetry (TGA-DSC) for MnO/NC and MnO_x/NC in air. The exothermic weight increase of MnO/NC starting from *ca.* 200 °C corresponded to the surface oxidation of MnO. The other exothermic peak at 300 °C was ascribed to the oxidation of carbon. In both materials, NC accounted for ~20 wt% of the hybrid, with 80 wt% MnO_x (see Fig. S1†).

The powder X-ray diffraction (XRD) affirmed the surface oxidation in MnO_x/NC (see Fig. 2a). MnO is the main component as a result of the carbon reducing effect at 900 °C. The manganese oxide recrystallized after the oxidation, showing broadened peaks in MnO_x/NC. New peaks also appeared, pertaining to the formation of Mn_3O_4 and MnO_2 (the XRD data of MnNTA are shown in Fig. S2†). We also ran temperature programmed reduction measurements in hydrogen (H_2-TPR, see Fig. S3†). MnO/NC showed little hydrogen consumption because MnO was irreducible in 5% H_2 up to 800 °C.[38] Conversely, MnO_x/NC showed several distinct reduction peaks, suggesting that the surface of MnO_x was indeed oxidized during the 200 °C-oxidation step (*vide infra*).

N_2-Adsoprtion measurements on the MnO_x/NC hybrid revealed a type-IV isotherm with an adsorption–desorption hysteresis loop (see Fig. 2b). The specific surface area was 135 m^2 g^{-1}. The pore volume reached 0.48 cm^3 g^{-1}, comparable with those porous materials derived *via* either "soft-templating" or "hard-templating" methods.[39–42] Calculating the micropore size distribution using the Horváth–Kawazoe (HK) model, we found that the median pore diameter was 0.84 nm (see Fig. 2c). Calculations using the Barrett–Joyner–Halenda (BJH) method revealed a mesopore size distribution ranging from 3.5 to 22 nm (see Fig. 2d). Alternatively, the pore size distribution obtained from the NLDFT method is shown in Fig. S4,† which revealed similar characteristics of the pore.

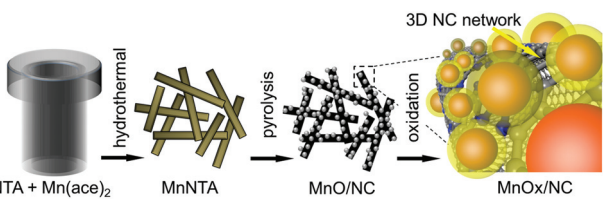

Fig. 1 A schematic synthesis procedure of the hierarchically porous MnO_x/NC nanorods catalyst. The hydrothermal, pyrolysis and oxidation treatments were carried out at 180 °C, 900 °C and 200 °C, respectively. The hybrid contained 20% NC and 80% MnO_x.

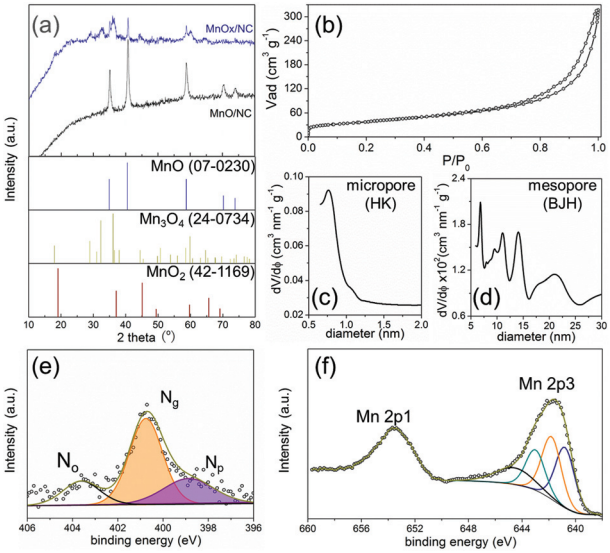

Fig. 2 Physical characterization of the MnO_x/NC hybrid: (a) XRD pattern and the standard patterns of MnO, Mn_3O_4 and MnO_2. The values in the parentheses are the JCPDS card numbers; (b) nitrogen adsorption isotherm and the pore size distribution in the regions of (c) micropores, calculated by the Horváth–Kawazoe method and (d) mesopores, calculated by the Barrett–Joyner–Halenda method; (e) deconvoluted XPS spectra of the N 1s core-level, N_p, N_g and N_o represent pyridinic, graphitic and oxidized nitrogen moieties, respectively, and (f) XPS spectra showing the Mn 2p core-level.

Note that the mesopore volume was up to 0.32 cm^3 g^{-1}, accounting for 67% of the total pore volume. Thus, this hierarchically porous structure meets the two requirements of a good electrocatalyst: efficient mass transfer and a large surface area with abundant active sites.[28,35–37]

We then used X-ray photoelectron spectroscopy (XPS) to examine the electronic structure of MnO_x/NC (see the survey spectrum in Fig. S5†). The carbon matrix in the hybrid had a high content of nitrogen, demonstrating a N/C ratio close to 6.4 at%. The spectrum of the N 1s core-level displayed three distinct nitrogen moieties. Of these, 28 at% were pyridinic (N_p) with a binding energy of 398.8 eV, which are believed to be the main active ORR sites.[43] The peaks at 400.7 eV and 401.6 eV were assigned to graphitic (N_g) and oxidized (N_o) nitrogen, respectively. The Mn $2p_{3/2}$ core-level spectrum in Fig. 2f shows a broad shake-up satellite peak at 644.6 eV and reveals the mixed valence of Mn on the surface. The peaks at 640.8 eV, 641.8 eV and 643 eV were assignable to Mn^{2+} (37.0%), Mn^{3+} (38.3%) and Mn^{4+} (24.7%), respectively.[24,44,45] Particularly, the latter two species were recognized to be critical in oxygen catalysis.[46] This also in turn proved the successful surface oxidation of MnO_x.

We also examined the morphologies of MnO_x/NC. Fig. 3a and b contrast the scanning electron microscopy (SEM) images of the MnNTA salt and MnO_x/NC. The rod-like shape remained stable after the pyrolysis and oxidation steps. The diameter of the rod was *ca.* 200 nm whereas the length was up to 3 μm. Interestingly, this structure was not observed when either Fe or

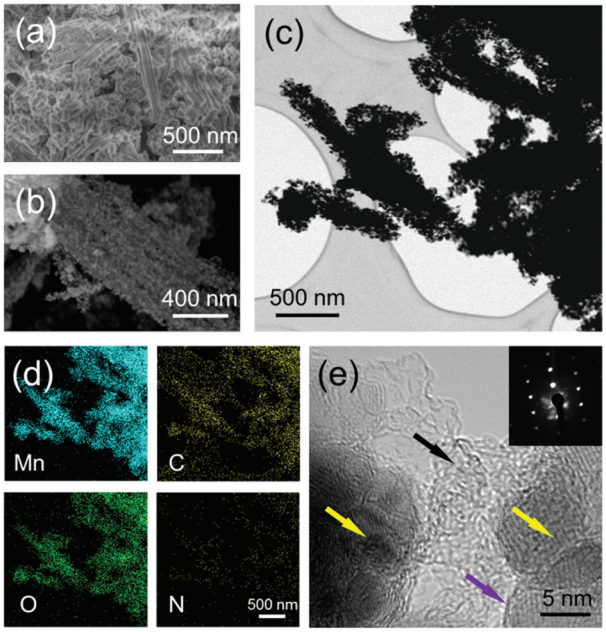

Fig. 3 SEM images of (a) MnNTA salt and (b) MnO_x/NC; (c) TEM image of MnO_x/NC nanorods and (d) the corresponding EDS elemental mappings; (e) HRTEM micrograph of the MnO_x/NC hybrid, wherein the black, yellow and purple arrows indicate the NC, MnO and amorphous MnO_x; the inset shows the SAED diffractogram of a MnO_x nanoparticle.

Mg was used instead of Mn (*cf.* Fig. S6†).[28,29] Fig. 3c shows the transmission electron microscopy (TEM) image. The nanorod structure was covered with a "furry" surface which was then confirmed as the uniformly distributed manganese oxide nanoparticles, typically with a size of 20 nm (see Fig. S7†). The corresponding elemental mappings in Fig. 3d from the energy-dispersive X-ray spectroscopy (EDS) confirm the homogeneous dispersion of both MnO_x and NC species in the hybrid (note that the carbon grid was also shown). This is important for electrocatalysis: the contiguous NC matrix connects the MnO_x nanoparticles (which are poor conductors themselves), increasing the electrical conductivity of the catalyst.

The high resolution TEM micrograph (HRTEM) in Fig. 3e shows the advantageous microstructure of the hybrid catalyst. The black arrow indicates that the NC serves as an electronic connector, bridging two MnO_x nanoclusters. Worm-like structures were seen, typically representing micropores in carbon materials, which enhanced the surface area; the mesopores originated from the inter-particle cavities, which created channels for the mass transport to and from the active sites. Importantly, the micropores and mesopores are all connected, offering a classic hierarchically porous structure. The diffractogram inset from the selected area electron diffraction (SAED) implied the single crystal of MnO. Nevertheless, amorphous MnO_x species were observed on the surface (*cf.* the XRD, H_2-TPR and XPS data). This amorphous structure might also be beneficial in the oxygen electrocatalysis.[33]

The electrocatalytic activities of MnO_x/NC and the controls were all evaluated in 0.1 M KOH electrolyte using a standard rotating disc electrode (RDE; detailed experimental procedures are included in the ESI†). In the ORR experiments, the cyclic voltammetry of MnO_x/NC in the N_2-staurated electrolyte showed no redox peaks (Fig. S8†). In contrast, a remarkable reduction peak was seen when switching to the O_2-saturated electrolyte, confirming that the oxygen reduction has occurred on the electrode. Subsequently, we performed linear sweep voltammetry (LSV) while varying the rotating speed of the RDE, a common approach for investigating the electrochemical reaction mechanism. In all cases from 400 rpm to 2400 rpm, high limiting-current densities were achieved and the onset potentials remained identical (Fig. 4a). The Koutecký–Levich plots in Fig. 4b were perfectly linear. Their slopes were all constant, from which the calculation indicated the preferable $4e^-$-transfer pathway of ORR catalyzed by the MnO_x/NC hybrid. In addition, MnO_x/NC demonstrated excellent robustness and resistance against methanol poisoning, superior to the commercial Pt/C catalyst. In the chronoamperometric measurements, no significant current loss was recorded after the methanol injection and 80% current was retained after the 10 h test (see Fig. S9†).

Fig. 4c compares the LSV of various catalysts. In the controls, the NC catalyst contained an essentially identical ratio of doped nitrogen with the counterpart in MnO_x/NC, whereas the MnO_x/C was formed by mixing MnO_x nanorods with carbon black (see the ESI† for details). The onset ($E_{orr\text{-}onset}$) and half-wave ($E_{orr\text{-}1/2}$) potentials are listed in Table 1, which are two important parameters for evaluating the activities of ORR catalysts. In general, both MnO_x/NC and MnO_x/C showed high $E_{orr\text{-}onset}$ at 0.95 V (all values are given *vs.* RHE), ranking them among the best Mn-based ORR catalysts to date (see Tables S1 and S2†). This also implied the beneficial features of MnO_x with the unique rod-structure and the mixed Mn valence. However, MnO_x/NC had a much higher $E_{orr\text{-}1/2}$ (0.80 V *vs.*

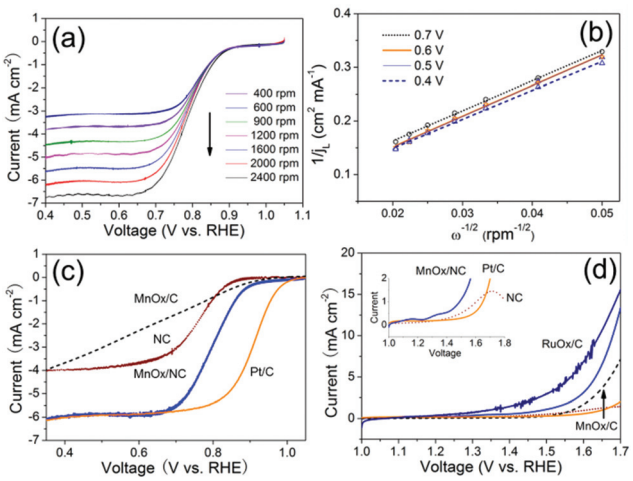

Fig. 4 (a) Linear sweep voltammetry at different rotating speeds and (b) the corresponding Koutecký–Levich plots of MnO_x/NC in ORR; a LSV comparison of various catalysts at 1600 rpm in (c) ORR and (d) OER. All the voltammograms were reordered with iR correction in oxygen-saturated 0.1 M KOH; the scan rate was 10 mV s^{-1}.

Table 1 Bifunctional activity comparison of different catalysts

Catalyst	$E_{orr\text{-}onset}$/V	$E_{orr\text{-}1/2}$/V	$E_{oer\text{-}onset}$/V	$E_{oer\text{-}10}$/V	ΔE^a/V
MnO_x/NC	0.95	0.80	1.41	1.67	0.87
NC	0.91	0.75	1.40	N.A.[b]	N.A.
MnO_x/C	0.95	0.64	1.45	>1.70	>1.06
Pt/C	1.04	0.91	1.5	1.90	0.99
RuO_2/C	0.81	0.69	1.30	1.64	0.95

[a] $\Delta E = E_{oer\text{-}10} - E_{orr\text{-}1/2}$. [b] NC underwent oxidation at high OER potentials.

0.64 V), suggesting the synergistic effects between the constituents. Cooperative catalysis might be indeed contributing as the NC was also a good ORR catalyst ($E_{orr\text{-}1/2}$ = 0.75 V).[24,47] More remarkably, the 20 wt% NC was contiguous, connecting every individual MnO_x nanoparticle that was much less conductive. Hence, with a larger quantity of MnO_x (>80 wt%) than those derived from conventional infiltration methods,[19,44] this hybrid had more electrochemically "valid" active sites (see the discussions and the structural comparison in Fig. S10†). Moreover, the resulting hierarchical porosity aligned with the superior electrical conductivity also granted good activity (see above).

We then investigated the OER activity of MnO_x/NC. As the state-of-the-art, RuO_2/C possesses the lowest OER onset potential ($E_{oer\text{-}onset}$) and the "benchmark" potential at 10 mA cm^{-2} ($E_{oer\text{-}10}$). Pt/C performed badly in accordance with the literature,[13,15,48,49] although DFT calculation suggested it might be as active as Ir oxide in OER.[48] Apparently, NC was unsuitable for OER in this study, suffering an instant passivation/oxidation at ~1.7 V (see the inset in Fig. 4d). In contrast, MnO_x/NC worked nicely thanks to its unique microstructure. Its $E_{oer\text{-}10}$ attained 1.67 V and the Tafel slope was 56 mV dec^{-1} (Fig. S11†), comparable to those of the recently-reported OER catalysts (*vide infra*).[50,51]

A good bifunctional catalyst must have a low voltage gap ($\Delta E = E_{oer\text{-}10} - E_{orr\text{-}1/2}$) between ORR and OER. This is especially crucial for applications in reversible fuel cells and rechargeable batteries. Excitingly, the ΔE of our MnO_x/NC was merely 0.87 V, outperforming that of both Pt/C and RuO_2/C. Starting from simple precursors *via* a facile approach, the obtained catalyst was also one of the best bifunctional catalysts reported to date (see Table S2† for comparison). As we discussed above and proved *via* the control experiments, the unique MnO_x–NC hybrid structure was the key factor contributing to the bifunctional excellence.

Conclusions

In summary, using two simple precursors and a scalable method, we developed a green and facile synthesis of hierarchically porous MnO_x/NC hybrid nanorods for efficient bifunctional oxygen catalysis. A small amount of a percolated NC network led to the formation of a porous structure, remarkably enhancing the conductivity and mass transfer in electrocatalysis. The mixed oxidation states of Mn cations along with the high ratio of nitrogen dopants contributed to the superior activity in both ORR and OER. The fact that this highly active bifunctional catalyst contains no noble metals aligned with a facile/green synthesis approach opens bona fide opportunities for the applications in new energy devices.

Acknowledgements

This work is part of the Research Priority Area Sustainable Chemistry of the UvA, http://suschem.uva.nl.

Notes and references

1 H. H. Tsai, W. Y. Nie, J. C. Blancon, C. C. S. Toumpos, R. Asadpour, B. Harutyunyan, A. J. Neukirch, R. Verduzco, J. J. Crochet, S. Tretiak, L. Pedesseau, J. Even, M. A. Alam, G. Gupta, J. Lou, P. M. Ajayan, M. J. Bedzyk, M. G. Kanatzidis and A. D. Mohite, *Nature*, 2016, **536**, 312–316.
2 Y. Guo, Y. T. Xu, B. Zhao, T. Wang, K. Zhang, M. M. F. Yuen, X. Z. Fu, R. Sun and C. P. Wong, *J. Mater. Chem. A*, 2015, **3**, 13653–13661.
3 N. Yan, J. Pandey, Y. M. Zeng, B. S. Amirkhiz, B. Hua, N. J. Geels, J. L. Luo and G. Rothenberg, *ACS Catal.*, 2016, **6**, 4630–4634.
4 G. Girishkumar, B. McCloskey, A. C. Luntz, S. Swanson and W. Wilcke, *J. Phys. Chem. Lett.*, 2010, **1**, 2193–2203.
5 D. J. Chen, C. Chen, Z. M. Baiyee, Z. P. Shao and F. Ciucci, *Chem. Rev.*, 2015, **115**, 9869–9921.
6 Z. Y. Lu, W. W. Xu, J. Ma, Y. J. Li, X. M. Sun and L. Jiang, *Adv. Mater.*, 2016, **28**, 7155–7161.
7 S. Lee, G. Nam, J. Sun, J. S. Lee, H. W. Lee, W. Chen, J. Cho and Y. Cui, *Angew. Chem., Int. Ed.*, 2016, **55**, 8599–8604.
8 C. Li, X. Han, F. Cheng, Y. Hu, C. Chen and J. Chen, *Nat. Commun.*, 2015, **6**, 7345.
9 L. C. Seitz, C. F. Dickens, K. Nishio, Y. Hikita, J. Montoya, A. Doyle, C. Kirk, A. Vojvodic, H. Y. Hwang, J. K. Norskov and T. F. Jaramillo, *Science*, 2016, **353**, 1011–1014.
10 G. Niu, M. Zhou, X. Yang, J. Park, N. Lu, J. Wang, M. J. Kim, L. Wang and Y. Xia, *Nano Lett.*, 2016, **16**, 3850–3857.
11 O. Groger, H. A. Gasteiger and J. P. Suchsland, *J. Electrochem. Soc.*, 2015, **162**, A2605–A2622.
12 Z. X. Wu, Y. Y. Lv, Y. Y. Xia, P. A. Webley and D. Y. Zhao, *J. Am. Chem. Soc.*, 2012, **134**, 2236–2245.
13 J. Masa, W. Xia, I. Sinev, A. Q. Zhao, Z. Y. Sun, S. Grutzke, P. Weide, M. Muhler and W. Schuhmann, *Angew. Chem., Int. Ed.*, 2014, **53**, 8508–8512.
14 A. Aijaz, J. Masa, C. Rosler, W. Xia, P. Weide, A. J. R. Botz, R. A. Fischer, W. Schuhmann and M. Muhler, *Angew. Chem., Int. Ed.*, 2016, **55**, 4087–4091.
15 S. Gadipelli, T. Zhao, S. A. Shevlin and Z. Guo, *Energy Environ. Sci.*, 2016, **9**, 1661–1667.

16 W. T. Hong, M. Risch, K. A. Stoerzinger, A. Grimaud, J. Suntivich and Y. Shao-Horn, *Energy Environ. Sci.*, 2015, **8**, 1404–1427.
17 B. Hua, Y. Q. Zhang, N. Yan, M. Li, Y. F. Sun, J. Chen, J. Li and J. L. Luo, *Adv. Funct. Mater.*, 2016, **26**, 4106–4112.
18 Z. H. Zhang, J. Liu, J. J. Gu, L. Su and L. F. Cheng, *Energy Environ. Sci.*, 2014, **7**, 2535–2558.
19 D. Jeong, K. Jin, S. E. Jerng, H. Seo, D. Kim, S. H. Nahm, S. H. Kim and K. T. Nam, *ACS Catal.*, 2015, **5**, 4624–4628.
20 W. H. Wang, J. Geng, L. Kuai, M. Li and B. Y. Geng, *Chem. – Eur. J.*, 2016, **22**, 9909–9913.
21 R. W. Chen, J. Yan, Y. Liu and J. H. Li, *J. Phys. Chem. C*, 2015, **119**, 8032–8037.
22 M. Huynh, C. Y. Shi, S. J. L. Billinge and D. G. Nocera, *J. Am. Chem. Soc.*, 2015, **137**, 14887–14904.
23 K. X. Lei, X. P. Han, Y. X. Hu, X. Liu, L. Cong, F. Y. Cheng and J. Chen, *Chem. Commun.*, 2015, **51**, 11599–11602.
24 J. Kang, H. Wang, S. Ji, J. Key and R. F. Wang, *J. Power Sources*, 2014, **251**, 363–369.
25 Z. H. Cui and X. X. Guo, *J. Power Sources*, 2014, **267**, 20–25.
26 W. Y. Wong, W. R. W. Daud, A. B. Mohamad, A. A. H. Kadhum, K. S. Loh and E. H. Majlan, *Int. J. Hydrogen Energy*, 2013, **38**, 9370–9386.
27 Y. Zheng, Y. Jiao, M. Jaroniec, Y. G. Jin and S. Z. Qiao, *Small*, 2012, **8**, 3550–3566.
28 D. Eisenberg, W. Stroek, N. J. Geels, C. S. Sandu, A. Heller, N. Yan and G. Rothenberg, *Chem. – Eur. J.*, 2016, **22**, 501–505.
29 D. Eisenberg, W. Stroek, N. J. Geels, S. Tanase, M. Ferbinteanu, S. J. Teat, P. Mettraux, N. Yan and G. Rothenberg, *Phys. Chem. Chem. Phys.*, 2016, **18**, 20778–20783.
30 Y. Yi, J. Tornow, E. Willinger, M. G. Willinger, C. Ranjan and R. Schlogl, *ChemElectroChem*, 2015, **2**, 1929–1937.
31 R. Mohamed, X. Cheng, E. Fabbri, P. Levecque, R. Kotz, O. Conrad and T. J. Schmidt, *J. Electrochem. Soc.*, 2015, **162**, F579–F586.
32 Y. T. Meng, W. Q. Song, H. Huang, Z. Ren, S. Y. Chen and S. L. Suib, *J. Am. Chem. Soc.*, 2014, **136**, 11452–11464.
33 A. Indra, P. W. Menezes, N. R. Sahraie, A. Bergmann, C. Das, M. Tallarida, D. Schmeisser, P. Strasser and M. Driess, *J. Am. Chem. Soc.*, 2014, **136**, 17530–17536.
34 J. X. Feng, H. Xu, Y. T. Dong, S. H. Ye, Y. X. Tong and G. R. Li, *Angew. Chem., Int. Ed.*, 2016, **55**, 3694–3698.
35 K. L. Pickrahn, S. W. Park, Y. Gorlin, H. B. R. Lee, T. F. Jaramillo and S. F. Bent, *Adv. Energy Mater.*, 2012, **2**, 1269–1277.
36 D. M. Kang, Q. L. Liu, R. Si, J. J. Gu, W. Zhang and D. Zhang, *Carbon*, 2016, **99**, 138–147.
37 L. Xu, Q. Q. Jiang, Z. H. Xiao, X. Y. Li, J. Huo, S. Y. Wang and L. M. Dai, *Angew. Chem., Int. Ed.*, 2016, **55**, 5277–5281.
38 D. Jampaiah, S. J. Ippolito, Y. M. Sabri, J. Tardio, P. R. Selvakannan, A. Nafady, B. M. Reddy and S. K. Bhargava, *Catal. Sci. Technol.*, 2016, **6**, 1792–1803.
39 F. Zhang, C. Liang, X. Wu and H. Li, *Angew. Chem., Int. Ed.*, 2014, **126**, 8638–8642.
40 W. Zhang, Q. X. Wang, H. H. Wu, P. Wu and M. Y. He, *Green Chem.*, 2014, **16**, 4767–4774.
41 J. Tang, J. Liu, C. L. Li, Y. Q. Li, M. O. Tade, S. Dai and Y. Yamauchi, *Angew. Chem., Int. Ed.*, 2015, **54**, 588–593.
42 H. Zhang, O. Noonan, X. Huang, Y. Yang, C. Xu, L. Zhou and C. Yu, *ACS Nano*, 2016, **10**, 4579–4586.
43 D. H. Guo, R. Shibuya, C. Akiba, S. Saji, T. Kondo and J. Nakamura, *Science*, 2016, **351**, 361–365.
44 Q. W. Tang, L. H. Jiang, J. Liu, S. L. Wang and G. Q. Sun, *ACS Catal.*, 2014, **4**, 457–463.
45 M. Piumetti, D. Fino and N. Russo, *Appl. Catal., B*, 2015, **163**, 277–287.
46 A. S. Ryabova, F. S. Napolskiy, T. Poux, S. Y. Istomin, A. Bonnefont, D. M. Antipin, A. Y. Baranchikov, E. E. Levin, A. M. Abakumov, G. Kerangueven, E. V. Antipov, G. A. Tsirlina and E. R. Savinova, *Electrochim. Acta*, 2016, **187**, 161–172.
47 J. K. Lee, M. C. Kung and H. H. Kung, *Top. Catal.*, 2008, **49**, 136–144.
48 T. Reier, M. Oezaslan and P. Strasser, *ACS Catal.*, 2012, **2**, 1765–1772.
49 J. I. Jung, H. Y. Jeong, J. S. Lee, M. G. Kim and J. Cho, *Angew. Chem., Int. Ed.*, 2014, **53**, 4582–4586.
50 Y. Li, L. Zhang, X. Xiang, D. P. Yan and F. Li, *J. Mater. Chem. A*, 2014, **2**, 13250–13258.
51 R. Gao, H. Zhang and D. P. Yan, *Nano Energy*, 2017, **31**, 90–95.